Out-of-plane growth of CNTs on graphene for supercapacitor applications

Youn-Su Kim, Kitu Kumar, Frank T Fisher and Eui-Hyeok Yang

Department of Mechanical Engineering, Stevens Institute of Technology,
Castle Point on Hudson, Hoboken, NJ 07030, USA

E-mail: eyang@stevens.edu

Abstract
This paper describes the fabrication and characterization of a hybrid nanostructure comprised of carbon nanotubes (CNTs) grown on graphene layers for supercapacitor applications. The entire nanostructure (CNTs and graphene) was fabricated via atmospheric pressure chemical vapor deposition (APCVD) and designed to minimize self-aggregation of the graphene and CNTs. Growth parameters of the CNTs were optimized by adjusting the gas flow rates of hydrogen and methane to control the simultaneous, competing reactions of carbon formation toward CNT growth and hydrogenation which suppresses CNT growth via hydrogen etching of carbon. Characterization of the supercapacitor performance of the CNT–graphene hybrid nanostructure indicated that the average measured capacitance of a fabricated graphene–CNT structure was $653.7 \ \mu\text{F cm}^{-2}$ at $10 \ \text{mV s}^{-1}$ with a standard rectangular cyclic voltammetry curve. Rapid charging–discharging characteristics (mV s^{-1}) were exhibited with a capacitance of approximately 75% ($490.3 \ \mu\text{F cm}^{-2}$). These experimental results indicate that this CNT–graphene structure has the potential towards three-dimensional (3D) graphene–CNT multi-stack structures for high-performance supercapacitors.

(Some figures may appear in colour only in the online journal)

1. Introduction

Electric double-layer capacitors (EDLCs) are promising energy storage devices having high power density (e.g. $\sim 14 \ \text{kW kg}^{-1}$), fast charge storage (rate capability) and stable cycle life (e.g. over 10^5) by means of charge accumulation at the interface of the electrode and electrolyte [1–3]. Thus, high surface area and low intrinsic resistance are vital for high performance [4–6]. Morphology-modified carbon nanostructures [7–11] such as activated carbon (AC), mesoporous carbon (MC) and carbon nanotubes (CNTs) have large surface areas, yet suffer from limited performance due to micropores and internal resistance, and therefore exhibit lower capacitance than theoretically predicted [4, 5, 12, 13]. On the other hand, graphene has recently been identified as a promising material for supercapacitor applications, due to its outstanding theoretical specific surface area (SSA) ($\sim 2630 \ \text{m}^2 \ \text{g}^{-1}$) [14], extraordinary electrical properties in the planar direction (sheet resistance $= \sim 280 \ \Omega \ \text{cm}^{-2}$) [15, 16], high mechanical strength (Young's modulus $= \sim 1.0 \ \text{TPa}$) [17] and chemical stability [18]. In addition, graphene exhibits

an intrinsic capacitance of up to $21 \ \mu\text{F cm}^{-2}$, the theoretical limit of carbon materials [19]. Recent successful development of chemical vapor deposition (CVD)-based graphene synthesis techniques facilitates the application of graphene as electrodes in lithium ion batteries and supercapacitors as well as electronics applications on metal substrates [20, 21]. However, supercapacitors composed of graphene alone still suffer from a loss of active surface area due to aggregation of the material [12, 13, 22]. While graphene–CNT [22–24] and graphene–polymer [12, 25] composites have been fabricated towards three-dimensional (3D) nanostructures, initial results still demonstrate overlapping and aggregation, due to the use of thick, aggregated graphene flakes or CNT bundles. This aggregation leads to a loss of available surface area and a reduction in supercapacitor performance [23].

To overcome the aforementioned limitations of aggregation and intrinsic resistance, we have fabricated and characterized a CNT–graphene supercapacitor, in which CNTs are grown directly out-of-plane from the graphene layers as illustrated schematically in figure 1. This structure is intended to minimize self-aggregation, while achieving low intrinsic
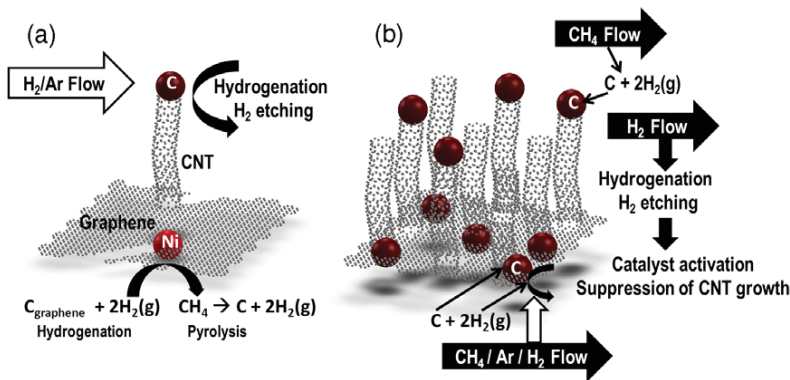
Figure 1. Schematics illustrating direct CNT growth on planar graphene (a) without carbon (methane) feedstock gas; here graphene is consumed and converted to methane via hydrogenation using Ni nanoparticles as catalyst. (b) Growth with methane feedstock: here the pyrolysis of methane supplies carbon and hydrogen to the system.

resistance between the CNTs and graphene layers. Additionally, the hybrid nanostructure geometry proposed here orients conductivity paths in the planar direction for graphene and axial direction of the CNTs, where resistance is minimal [26]. Unlike CNT growth on conventional substrates (Si, SiO$_2$), here 'direct' CNT growth out of graphene can only be facilitated by a controlled suppression of carbon etching. Two simultaneous, competing reactions occur during CNT growth on graphene. The first is carbon (CNT) growth out of metal catalyst islands. The second is hydrogenation, that is, the reaction of ambient H$_2$ with the carbon growth in the presence of a catalyst to form methane (CH$_4$) gas, which results in an etching of the graphene substrate. Thus, in this paper, we investigate the process parameters and growth mechanisms of the proposed hybrid nanostructure comprised of CNTs grown on graphene layers to find the optimal range of parameters where the rate of carbon growth is not overwhelmed by the hydrogenation rate. Lastly, we characterize the electrochemical performance of the hybrid nanostructure via cyclic voltammetry to demonstrate one potential application of this material as a supercapacitor.

2. Large-area graphene fabrication

Graphene layers were grown on Cu foil (99.99% purity) by atmospheric pressure chemical vapor deposition (APCVD). A Cu scroll (size: 13×60 cm^2) was placed in the center of a 2 inch diameter quartz tube in a horizontal three-zone tube furnace and heated to 1000 °C under H$_2$ and argon (Ar) flow. High temperature annealing was then carried out to increase the grain size of the Cu foil, which has been shown to lead to high quality graphene films with large grain size [27, 28]. Next, reaction gas mixtures of CH$_4$, H$_2$ and Ar were fed through the system at flow rates of 50, 15 and 1000 sccm, respectively, for 4 min of graphene growth. Subsequently, the sample was rapidly cooled down to room temperature under H$_2$ and Ar, resulting in graphene layers grown on both sides of the Cu foil. To transfer the grown layers to the desired substrates, the Cu foil was first partially etched in a magnetically stirred 0.1 M FeCl$_3$ solution to remove the bottom-side graphene growth. After several deionized (DI) water rinses, the Cu was fully

etched in a 0.1 M FeCl$_3$ bath without magnetic stirring. The isolated graphene film was then rinsed several times with DI water to remove the residual etchant before transfer onto a substrate.

For characterization of the as-grown graphene films on which the CNT forests would be grown, they were transferred onto either an oxidized Si substrate for Raman spectroscopy or a stainless steel substrate for electrochemical characterization. The adhesion between the graphene and the substrates are attributed to van der Waals forces [29], where no additional binders or clamps were needed to maintain good contact with the substrate. As shown in figures 2(a) and (b), Raman spectra taken from the transferred graphene films exhibit two distinctive peaks corresponding to the G band (1587.34 cm^{-1}) and 2D band (2693.70 cm^{-1}) of graphene. The characteristic D band at $\sim$1381 cm^{-1} is not present, which in the literature has been described as being indicative of near-defect-free graphene layers [30, 31]. The 2D band peak shows a higher peak intensity than the G band with a 2D to G intensity ratio $I_{2D}/I_G \sim 2.2$ and can be fitted with sharp, symmetric Lorentzian with a full width at half-maximum of 38.3 cm^{-1}.

3. Experimental results of CNT growth on graphene

3.1. Effect of catalyst density on CNT growth

To create CNT–graphene structures with a minimal aggregation, different techniques were pursued to facilitate out-of-plane growth of the CNTs on the graphene surface. Nickel (Ni) nanoparticles were synthesized on graphene as CNT growth catalysts using two different techniques, pulsed laser deposition (PLD) or dip-drawing, for comparison and optimization. Using PLD, an Ni film 5 nm thick was deposited on graphene with a laser power of 200 mW and repetition rate of 10 Hz at room temperature under 10^{-6} Torr pressure. The dip-drawing method was used to coat graphene with a catalyst solution; here the graphene substrate was dipped into a 0.2 mM NiCl$_2$/ethanol solution and then drawn out slowly [34]. Ni films or coatings created by either the PLD or dip-drawing techniques were then subjected to a thermal
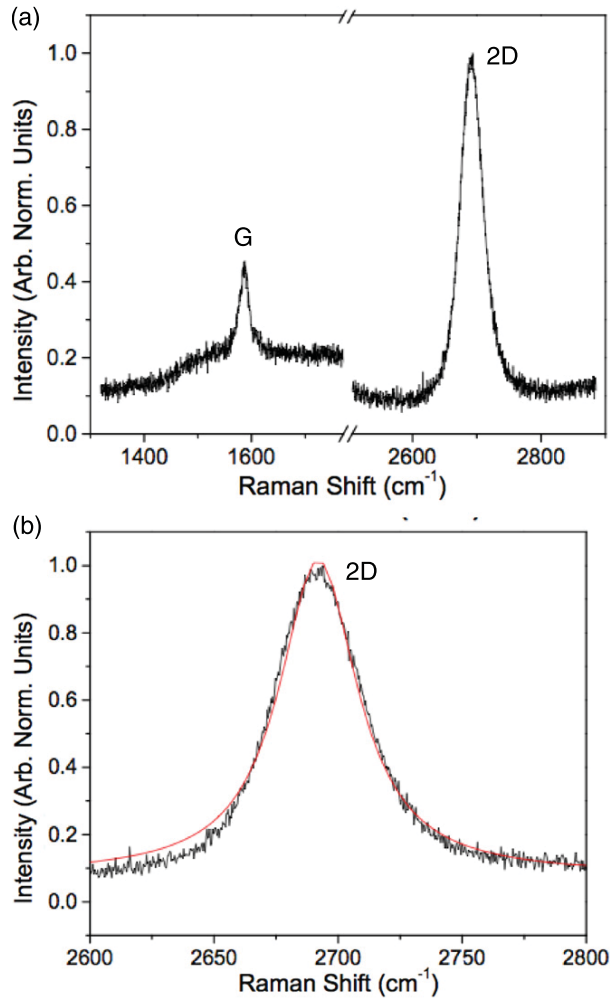
(a)

(b)

Figure 2. (a) Raman spectrum of CVD-grown graphene showing a G band (1587.34 cm^{-1}) and 2D band (2693.70 cm^{-1}) peaks. The 2D peak shows higher peak intensity than the G peak with a 2D to G intensity ratio $I_{2D}/I_G \sim 2.2$. (b) 2D peak with a sharp, symmetric single Lorentzian fit having a full width at half-maximum of 38.3 cm^{-1}, indicating that this film is few-layered graphene. For CVD-grown graphene, monolayer, bilayer and few-layer 2D spectra show one broadened peak rather than subcomponents since the stacking order is turbostratic (i.e. no Bernal stacking) [32, 33]. In order to precisely determine the number of layers in CVD-grown graphene, AFM or TEM characterization can calibrate the Raman data.

treatment to granulate the films into nanoparticles to be used as catalyst particles for CNT growth. Here samples were heated to 500 °C under Ar (99.999%, GTS Welco) gas flow (400 sccm), followed by H$_2$ (99.999%, GTS Welco) annealing (50 sccm), which causes the nanoparticle formation due to stresses caused by thermal expansion and H$_2$ etching [35, 36]. It was found that the PLD of Ni resulted in uniform formation of nanoparticles of approx. 30–70 nm diameter and tightly packed density of approx. 8.6×10^9 cm^{-2}. In contrast, Ni catalysts generated via dip-drawing displayed random dispersion on graphene and a wider variation in density and diameter as shown in the SEM images in figure 3(a). The size and density of the catalyst

Table 1. CVD gas flow rates and the resulting CVD phenomena (Ar, H$_2$ and CH$_4$ gases at 900 °C).

Gas flow (sccm)			
Ar	H$_2$	CH$_4$	CVD phenomena
850	150	0	Graphene etching and growth of short CNTs
850	150	20	CNT growth
850	150	50	CNTs with low density
850	150	100	Low density of short CNTs
850	0	100	Thick carbon film
950	50	100	CNT growth

nanoparticles are critical for growth of vertically aligned CNTs because van der Waals interaction between neighboring CNTs are a major driving force for an aligned growth [37, 38]. Since a higher degree of uniformity was achieved using the PLD-based nanocatalyst growth, the majority of the results presented below focuses on results obtained using the PLD technique for the creation of the Ni nanoparticles catalysts for CNT growth on graphene.

3.2. CNT growth process

Prior to CNT growth, the thermal treatment process described above was performed on the Ni film-covered graphene to form Ni nanoparticles. The furnace temperature was then increased to 900 °C under Ar and H$_2$ flow [39]. At the reaction temperature of 900 °C, a mixture of CH$_4$ (99.97%, GTS Welco), H$_2$ and Ar gases was fed through the furnace for CNT growth on graphene via the vapor–liquid–sold (VLS) process. The reaction gas flow rates of CH$_4$, H$_2$ and Ar were varied from 0–100, 50–150 and 850–950 sccm, respectively, to optimize the CNT growth conditions by balancing the competing processes of hydrogen etching and carbon formation on Ni catalysts [36, 39]. A summary of the results of the CNT growth process for various process gas flow rates is presented in table 1 and discussed in more detail in the following section. After the CNT growth on graphene layers was completed, the tube was cooled down to room temperature under Ar flow (400 sccm). Figures 3(c) and (d) shows representative SEM images of a CNT forest grown on a graphene substrate under mixed gas flow (Ar/H$_2$/CH$_4$ = 850/150/20 sccm) at 900 °C using dip-drawing coated (figure 3(a)) and PLD-deposited (figure 3(b)) Ni films, respectively. Comparison of the CNT Raman spectra shown in the inset of figure 3(d) to the graphene spectra (figure 2(a)) clearly indicates the presence of CNTs with the appearance of a shifted D peak at ∼1370 cm^{-1}, and the broadening and decreased intensity of the 2D peak at ∼2700 cm^{-1}. Additionally, the I_D/I_G ratio of 0.5 is similar to values reported of CNTs grown under CH$_4$ flow in the literature [39]. The morphology of CNTs synthesized via PLD-deposited Ni film exhibited a narrow diameter distribution (approx. 20–40 nm) owing to well-dispersed, high-density catalyst nanoparticles as shown in figure 3(b). CNTs grown from catalysts fabricated via the dip-drawn Ni film displayed a much larger range of diameters (approx. 5–40 nm) (verified using SEM images).
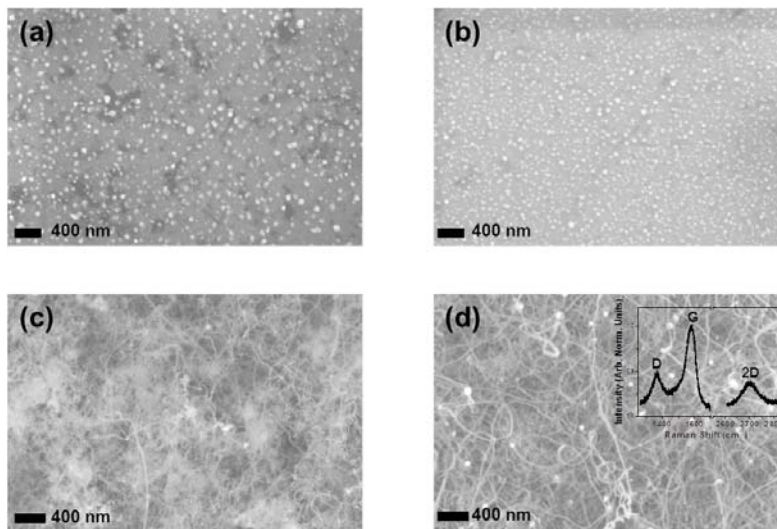
Figure 3. SEM images of Ni nanoparticle catalysts grown on graphene created via H_2 treatment of (a) dip-drawing coated Ni thin film on graphene and (b) PLD-deposited thin film on graphene. (c), (d) Graphene–CNT hybrid structures as grown from (a) and (b) using the dip-drawing and PLD methods, respectively. The inset in (d) shows the Raman spectra of CNTs grown on graphene. The I_D/I_G ratio of 0.5 is characteristic of CNTs grown using methane [39]. The CNTs were grown under mixed gas flow ($Ar/H_2/CH_4 = 850/150/20$ sccm) at 900 °C.

3.3. CNT growth parameter optimization

During the CNT growth process on the graphene substrate using Ni nanoparticle catalysts, carbon formation occurs by means of thermal decomposition of hydrocarbons ($C_nH_m \rightarrow nC + m/2H_2$) on the catalyst nanoparticles along with the catalyst activation due to the desorption of carbon fragments from the surface of catalyst by hydrogen etching. Therefore, the CNT growth process condition for the successful fabrication of graphene–CNT structures is largely influenced by the reaction gas flow conditions such as the presence of methane and variation of methane and hydrogen flow rates as illustrated earlier in table 1 and discussed in more detail below.

3.3.1. No-methane condition. CNTs can be directly grown from graphene without a feedstock gas, since graphene can act as a carbon source through the hydrogenation process [40, 41]. During hydrogenation, graphene is catalytically etched via H_2 and converted to methane at the point of contact with the metal nanoparticles ($Ni_{nanoparticle} + C_{graphene} + 2H_2 \rightarrow Ni + CH_4$) [34, 42]. Simultaneously, the methane is thermally decomposed and also acts as a carbon source for CNT growth. From these reactions, CNT growth without carbon feedstock ($Ar/H_2/CH_4 = 850/150/0$ sccm) occurs on low-density catalysts, such as those prepared by the dip-drawing method. Since CNTs precipitate only out of super-saturated catalysts, the ratio of the carbon source to catalyst must be high enough for this to occur. Thus, a low concentration nanoparticles array [41] is essential for CNT growth as the amount of carbon (supplied by the etched, or hydrogenated, graphene) is limited in the case of the no-methane process condition. Here, the hydrogenated methane acts as a second carbon source for CNT growth by decomposing into carbon and hydrogen at 900 °C. Using the

dip-drawing method, a low density of short CNTs is grown; density being related to the low density of catalyst particles and length having to do with the limited carbon supply and overwhelmingly greater rate of hydrogen (from bulk) etching of carbon. In the case of PLD-grown Ni catalysts, CNT growth does not occur as the ratio of catalyst to carbon source is too high for super-saturation of the Ni nanoparticles (inset of figure 4(a)). Because the concentration of carbon feedstock is low compared to the dense array of catalysts, a higher H_2-assisted carbon desorption rate [36] overwhelms the rate of carbon formation, thus maintaining high catalytic activity for the hydrogenation process and suppressing CNT growth.

3.3.2. Methane condition. In this section, we describe a parametric variation of flow rates in an effort to find the optimal CNT growth conditions on graphene. When catalytic CNT growth is accomplished by feeding CH_4 (accompanied by Ar and H_2) through the system, the catalysts are saturated with a high concentration of carbon. This saturation suppresses the catalytic activity of the nanoparticle and thus graphene etching via hydrogenation is suppressed. In our experiments, CH_4 flow rates were varied while Ar and H_2 flow rates were kept constant. As shown in figure 4(b), CNTs were grown on graphene using low concentration of CH_4 gas ($Ar/H_2/CH_4 = 850/150/20$ sccm), which indicates the rate of methane decomposition, carbon diffusion/formation and hydrogen etching are well optimized at the synthesis temperature (900 °C). An increased methane flow rate ($Ar/H_2/CH_4 = 850/150/50$ sccm) showed lower density and shorter CNTs (figure 4(c)) than those grown under low methane concentration ($CH_4 = 20$ sccm). Perhaps counterintuitively, these results illustrate that higher concentrations of methane can actually suppress CNT growth. However, these results can be attributed to the effects of
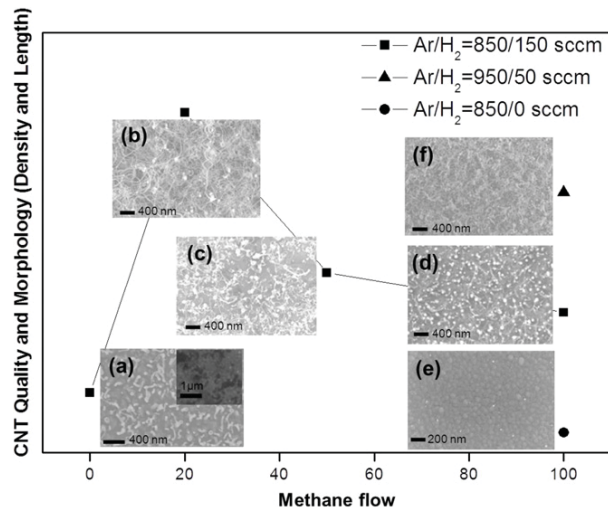
Figure 4. Quality and morphology of CNTs grown on graphene under varying growth conditions: (a)–(c) under varying methane flow (Ar/H_2 = 850/150 sccm) and (d)–(f): Ar = 950 sccm varying hydrogen flow (CH_4 = 100 sccm). Zero methane conditions ((a), 0 sccm) induce graphene to act as the carbon source, though in a limited quantity. It must be noted that the CNTs grown using this method are shorter in length because of the limited carbon source from finite graphene dimensions. Comparatively, only graphene etching was observed in the no-methane process using high-density catalyst arrays prepared by PLD (inset). Under intermediate methane conditions ((b), 20 sccm), the rate of methane decomposition, carbon diffusion/formation and hydrogen etching is well optimized, growing densely packed, long CNTs. At a higher methane flow rate ((c), 50 sccm), the dissociated H_2 from CH_4 acts as an etchant, overwhelming the rate of carbon formation and resulting in sparser and shorter CNTs than in (b). Under high methane flow and high hydrogen flow ((d), 100 sccm and 150 sccm, respectively), the rate of carbon formation is almost entirely overwhelmed by H_2 etching, leading to poor quality CNTs. Under zero hydrogen flow (e), methane decomposition and carbon diffusion/formation dominate and a layer of carbon coats the substrate. Under intermediate hydrogen flow ((f), 50 sccm), the rate of carbon formation and hydrogen etching are well optimized, leading to high quality CNT growth.

hydrogen etching on carbon during the CNT growth process; higher concentrations of hydrogen, relative to methane and argon gases, suppress the effects of carbon formation. The increase in hydrogen is generated by the pyrolysis of hydrocarbon [43], thus both sources of H_2 must be factored into the CNT growth process. By further increasing CH_4 flow rate ($Ar/H_2/CH_4$ = 850/150/100 sccm) during the CVD process (thus increasing the concentration of H_2), CNT growth was further suppressed and therefore low density of short CNTs were observed (figure 4(d)). These results strongly suggest that hydrogen etching, rather than thermal decomposition of methane, carbon transfer/diffusion and carbon formation on catalyst, is the critical factor in the given flow rate region to control the CNT growth quality and morphology.

3.3.3. Hydrogen effect. To further confirm this finding, the H_2 flow rate was varied (0, 50 and 150) under a high

concentration of CH_4 flow (100 sccm). A thick carbon layer was deposited on the entire graphene layer when only methane was fed ($Ar/H_2/CH_4$ = 850/0/100 sccm), indicating loss of catalytic activity of the nanoparticles due to high carbon content, and thus saturation and growth around the particles, caused by the pyrolysis of CH_4 at the growth temperature (figure 4(e)). With an intermediate H_2 gas flow rate ($Ar/H_2/CH_4$ = 950/50/100 sccm), CNTs were grown in high density on graphene, indicating that the hydrogen etching rate balanced the rate of carbon formation, allowing the CNTs to grow (figure 4(f)). Under high hydrogen flow ($Ar/H_2/CH_4$ = 850/150/100 sccm), the hydrogen etching effect was dominant and produced a low density of shorter CNTs.

Densely packed, long CNTs grown on planar graphene using methane imply large surface areas available for charge storage. This is more suitable to energy storage applications compared to the loosely packed, short CNTs and etched graphene arising from no-methane growth processes. Thus, we have narrowed the range of optimal parameters for out-of-plane CNT growth on graphene.

4. Electrochemical characterization of graphene–CNT supercapacitor

The electrochemical behavior of the fabricated graphene–CNT structure was characterized by cyclic voltammetry (CV). The experiments were carried out in a three-electrode glass cell. Here, the graphene–CNT structure was used as an electrode in a supercapacitor. For comparison of performance, a control graphene film (created using the procedures described in section 2, but not subjected to Ni particle coating or subsequent CNT growth) and a 1×1 cm^2 graphene–CNT structure were transferred onto stainless steel substrates, and each of them was used as a working electrode. The front- and back-side of the stainless steel substrate were fully covered by the graphene sample and a solid plastic cover, respectively. This cover minimized the stainless steel's exposure to the electrolyte. CV curves of stainless steel only (not shown here) also show minimal contribution to the overall capacitance. From our electrochemical tests, we observed the rectangular shape of the CV curve as shown in figure 5, which indicates that electron transfer occurs efficiently, implying that there is a good adhesion between the graphene and stainless steel. Platinum (Pt) foil was used as a counter electrode and Ag/AgCl (sat. KCl) as the reference electrode. CV measurements were performed within the potential range of 0.0–0.8 V at scan rates of 5–300 mV s^{-1}. Because of the small mass of graphene, the capacitances of the electrodes were calculated as a capacitance per area (F cm^{-2}) instead of the gravimetric value (F g^{-1}). The average capacitance was normalized per area of the samples and was estimated according to the following equation:

$$C_{average} = \frac{\int_{E1}^{E2} I(E)\,dE}{2(E2 - E1)vA}$$

where $I(E)$ is the instantaneous current, $E1$ and $E2$ are cutoff potentials in cyclic voltammetry, v is the potential scan rate and A is the area of the electrode. The measured cyclic
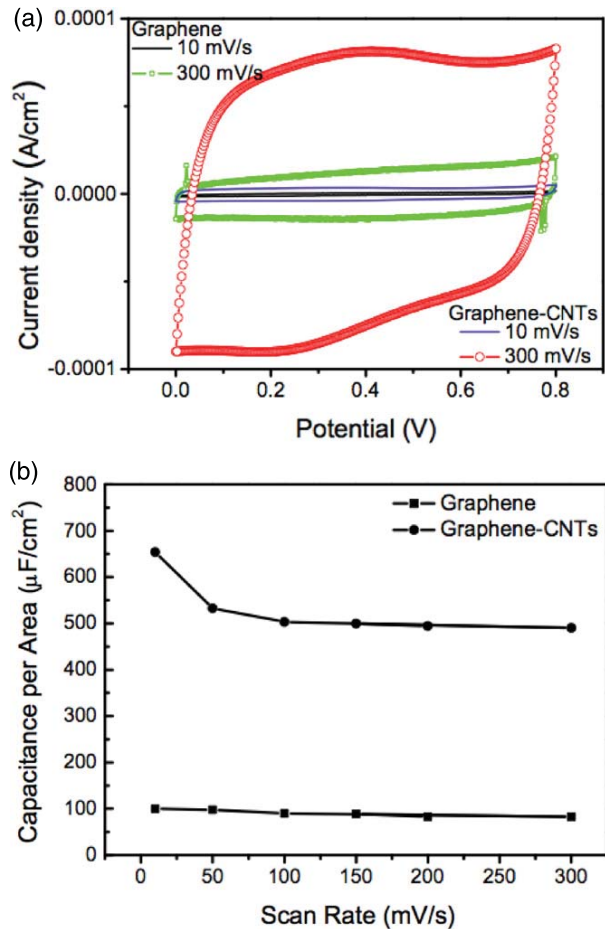
Figure 5. (a) Cyclic voltammograms at different scan rates in 0.1 M H_2SO_4 at room temperature and (b) capacitance per area obtained at scan rates of 10–300 mV s^{-1} for CVD-grown graphene without CNTs and graphene–CNT hybrid electrode.

voltammetry curves from both samples after approximately 100 cycles show a standard rectangular shape as shown in figure 5, indicating that electron transfer was not restricted during the accumulation of charged ions on the surface of the electrode. For both samples, oxidation and reduction peaks of Ni and Cu were also not present in the CV curve, which suggests that the effects of Ni nanoparticles used for CNT growth is negligible and that the Cu foil was fully etched and rinsed during the graphene transfer process. The CV curves of the graphene–CNT sample maintained a rectangular shape throughout the testing duration at exceedingly high scan rates of over 300 mV s^{-1}, which indicates that there is efficient electron transport during fast charging and discharging processes (i.e. low intrinsic resistance) [5, 7]. The measured average capacitance of the graphene–CNT sample was 653.7 μF cm^{-2} at 10 mV s^{-1}, which is considerably higher than that of the graphene-only electrode (99.6 μF cm^{-2} at 10 mV s^{-1}), attributed to the extra surface area provided by CNTs. Furthermore, the capacitance of a fabricated graphene–CNT sample was maintained at 490.3 μF cm^{-2} even at the charging and discharging rates of

300 mV s^{-1}, implying a very rapid current response on voltage reversal at each end potential [22, 24]. This indicates that the out-of-plane CNT structure grown on a non-aggregated graphene layer without micropores generates a stable, low-resistance electric interconnection between graphene and CNT. This points to the potential of the structure for future high-performance supercapacitors.

5. Summary

We have demonstrated the fabrication and characterization of a new class of hybrid structure of graphene and CNT for supercapacitor applications. The graphene layers (size: 13×60 cm^2) were synthesized on Cu foil via APCVD at 1000 °C and transferred on a desired substrate. The CVD-grown graphene showed a characteristic spectrum of few-layer graphene with single sharp Lorentz peak of 38.3 cm^{-1} at full width of the half-maximum (FWMH) and a 2D to G intensity ratio I_{2D}/I_G of 2.2. CNTs were then synthesized on this APCVD-grown graphene using Ni catalyst nanoparticles and an additional APCVD process. Out-of-plane CNTs were successfully grown on graphene by optimizing the rate of carbon formation, carbon transfer/diffusion and H$_2$ etching with flow rates of Ar:H$_2$:CH$_4$ = 850:150:20 and 850:50:100, at 900 °C. Careful optimization of the gas flow rates of hydrogen and methane was necessary to control the simultaneous, competing reactions of carbon formation towards CNT growth and hydrogenation which suppresses CNT growth via hydrogen etching of carbon. Lastly, we characterized the electrochemical performance of the graphene–CNT electrode. The hybrid electrode exhibits potential as a supercapacitor with a greater capacitance than the graphene-only electrode and maintains (490.3 μF cm^{-2}) capacitance under a fast charging–discharging process (300 mV s^{-1}). While several studies in the literature illustrate excellent supercapacitor performance based on CNT electrodes, realizing outstanding performance of graphene-based supercapacitors will require an approach that prevents the agglomeration of the graphene sheets. Here out-of-plane CVD-grown CNTs are used to vastly reduce graphene self-aggregation and concurrently act as current pathways which, given the high conductivity of both CNTs and graphene, is anticipated to facilitate electron transport throughout the structure during the charge–discharge process. Future work includes a detailed investigation of electrochemical performance of the hybrid nanostructure as a function of available surface area, lifecycle performance and the development of graphene–CNT–graphene 3D multi-stack as a stepping stone in creating high-performance supercapacitors.

References

[1] Simon P and Gogotsi Y 2008 *Nature Mater.* **7** 845
[2] Zhu Y *et al* 2011 *Science* **332** 1537
[3] Arepalli S *et al* 2005 *JOM* **57** 26
[4] Pandolfo A G and Hollenkamp A F 2006 *J. Power Source* **157** 11
[5] Fuertes A B, Pico F and Rojo J M 2004 *J. Power Source* **133** 329
[6] Yoon S, Lee C W and Oh S M 2010 *J. Power Sources* **195** 4391
[7] Zhang L L and Zhao X S 2009 *Chem. Soc. Rev.* **38** 2520
[8] Futaba D N, Hata K, Yamada T, Hiraoka T, Hayamizu Y, Kakudate Y, Tanaike O, Hatori H, Yumura M and IIjima S 2006 *Nature Mater.* **5** 987
[9] Zhang H, Cao G, Yang Y and Gu Z 2008 *J. Electrochem. Soc.* **155** K19
[10] Kim B, Chung H and Kim W 2010 *J. Phys. Chem.* C **114** 15223
[11] Du C and Pan Ning 2006 *Nanotechnology* **17** 5314
[12] Zhang K, Zhang L L, Zhao X S and Wu J 2010 *Chem. Mater.* **22** 1392
[13] Liu C, Yu Z, Neff D, Zhamu A and Jang B Z 2010 *Nano Lett.* **10** 4863
[14] Stoller M D, Park S, Zhu Y, An J and Ruoff R S 2008 *Nano Lett.* **8** 3498
[15] Kim K S, Zhao Y, Jang H, Lee S Y, Kim J M, Kim K S, Ahn J H, Kim P, Choi J Y and Hong B H 2009 *Nature* **457** 706
[16] Cai W, Zhu Y, Li X, Piner R D and Ruoff R S 2009 *Appl. Phys. Lett.* **95** 123115
[17] Lee C, Wei X, Kysar J W and Hone J 2008 *Science* **321** 385
[18] Blake P *et al* 2008 *Nano Lett.* **8** 1704
[19] Xia J, Chen F, Li J and Tao N 2009 *Nature Nanotechnol.* **4** 505
[20] Reddy A L M, Srivastava A, Gowda S R, Gullapalli H, Dubey M and Ajayan P M 2010 *ACS Nano* **4** 6337
[21] Yoo J J *et al* 2011 *Nano Lett.* **11** 1423
[22] Yu D and Dai L 2010 *J. Phys. Chem. Lett.* **1** 467
[23] Yang S Y, Chang K H, Tien H W, Lee Y F, Li S M, Wang Y S, Wang J Y, Ma C C M and Hu C C 2011 *J. Mater. Chem.* **21** 2374
[24] Cheng Q, Tang J, Ma J, Zhang H, Shinya N and Qin L-C 2011 *Phys. Chem. Chem. Phys.* **13** 17615
[25] Zhang L L, Zhao S, Tian X N and Zhao X S 2010 *Langmuir* **26** 17624
[26] Kondo D, Sato S and Awano Y 2008 *Appl. Phys. Express* **1** 074003
[27] Li X *et al* 2009 *Science* **324** 1312
[28] Bae S *et al* 2010 *Nature Nanotechnol.* **5** 574
[29] Reina A, Jia X, Ho J, Nezich D, Son H, Bulovic V, Dresselhaus M S and Kong J 2009 *Nano Lett.* **9** 30
[30] Li X *et al* 2010 *Nano Lett.* **10** 4328
[31] Saito R, Jorio A, Filho A G S, Dresselhaus G, Dresselhaus M S and Pimenta M A 2001 *Phys. Rev. Lett.* **88** 027401
[32] Ferrari A C *et al* 2006 *Phys. Rev. Lett.* **97** 187401
[33] Ismach A, Druzgalski C, Penwell S, Schwartzberg A, Zheng M, Javey A, Bokor J and Zhang Y 2010 *Nano Lett.* **10** 1542
[34] Ci L, Song L, Jariwala D, Elias A L, Gao W, Terrones M and Ajayan P M 2009 *Adv. Mater.* **21** 4487–91
[35] Siegal M P, Overmyer D L and Provencio P P 2002 *Appl. Phys. Lett.* **80** 2171
[36] Nessim G D, Hart A J, Kim J S, Acquaviva D, Oh J, Morgan C D, Seita M, Leib J S and Thompson C V 2008 *Nano Lett.* **8** 3587
[37] Fan S, Chapline M G, Franklin N R, Tombler T W, Cassell A M and Dai H 1999 *Science* **283** 512
[38] Bao Q and Pan C 2006 *Nanotechnology* **17** 1016
[39] Son S Y, Lee Y, Won S, Kim S D, Sung S W and Lee D H 2008 *Indust. Eng. Chem. Res.* **47** 2166
[40] Hunley D P, Johnson S L, Stieha J K, Sundararajan A, Meacham A T, Ivanov I N and Strachan D R 2011 *ACS Nano* **8** 6403
[41] Campos L C, Manfrinato V R, Sanchez-Yamagishi J D, Kong J and Jarillo-Herrero P 2009 *Nano Lett.* **9** 2600
[42] Datta S S, Strachan D R, Khamis S M and Johnson A T C 2008 *Nano Lett.* **8** 1912
[43] Zhang G *et al* 2005 *Proc. Natl Acad. Sci.* **102** 16141